5 Simulation of Active and Nonlinear Photonic Nano-Materials in the Finite-Difference Time-Domain (FDTD) Framework

A. Klaedtke, J. Hamm, and O. Hess

Advanced Technology Institute, School of Electronics and Physical Sciences,
University of Surrey, Guildford, Surrey, GU2 7XH, UK

Abstract. A numerical method is presented that unites three-dimensional finite-differnce time-domain (FDTD) computer simulations of active, nonlinear photonic nano-materials with optical Bloch equations describing their microscopic spatio-temporal dynamics. The constituent equations are derived and the algorithm is discussed. Computationally simulated Rabi oscillations closely correspond to analytic results. Fully three-dimensional simulations reveal the nonlinear spatio-temporal dynamics of high-finesse whispering gallery modes in microdisk lasers.

5.1 Introduction

With Moore's famous law still holding at the time of writing of this chapter, processors are getting faster and the main memory capacity of computers is increasing steadily. This opens up the possibility to refine physical models to a detailed level unthinkable several decades ago. Closely linked to this remarkable progress in the development of nano-structuring technologies in micro- and nano-electronics, novel photonic nano-materials and structures can be fabricated today that even carry functionalities on sub-wavelength scales.

Theoretical models for and computer simulation of photonic nano-materials often rely on well-known simplifications that profit from the assumption that all optical effects may be described on spatial scales that correspond to several times the optical wavelength. However, in the novel nano-photonic materials the typical structural variation are significantly smaller than the wavelength. In these cases (and even close to the wavelength) these simplifications can longer be made any more. Indeed, Maxwell's equations describing the spatio-temporal evolution of the electromagnetic field have to be considered in full detail. Compared with simpler models this enormously increases the computational complexity. Ironically, the steadily shrinking scales of novel electronic and photonic nano-structures make on the one hand computer simulations of their optical and materials properties more tedious but on the other hand provide the basis for the conception and realization of increasingly more powerful computing platforms on which the simulations run.

A. Klaedtke, J. Hamm, and O. Hess, Simulation of Active and Nonlinear Photonic Nano-Materials in the Finite-Difference Time-Domain Framework, Lect. Notes Phys. **642**, 75–101 (2004)
http://www.springerlink.com/

In this chapter we will first describe a well established combination of algorithms to solve the Maxwell curl equations with boundary conditions and discuss their implementation. The code snippets shown are in a pseudo programming language similar to C or C++. Subroutines are called without the global variables as parameters. In the second part of this report, a method is demonstrated which couples the optical Bloch equations in a special form to the electromagnetic field. The optical Bloch equations describe the quantum behaviour of a system interacting with the electric field on the basis of a dipole interaction Hamiltonian. With the resulting time-domain full vectorial Maxwell Bloch equations, the interplay of light with optically active nanomaterials can be computationally investigated.

5.2 Finite-Difference in Time-Domain

For the calculations involving the electromagnetic fields we will formulate the Maxwell curl equations in the so called Heaviside-Lorentz form. This unit system is conveniant to equalize the magnitude of the numerical values of the electric and magnetic field allowing higher precision when additions are performed on digital microprocessors using floating point numbers. Note that if we were using the MKSA system of units in contrast, we would introduce an imbalance with the dielectric constant of vacuum ϵ_0 and the permeability of vacuum μ_0 being of significantly different magnitude. Furthermore, we conveniently set the speed of light in vacuum c to 1.

Frequently, the Maxwell curl equations can be simplified taking the specific properties of the nano-materials into account. Considering non-magnetic materials results in the equivalence of the magnetic induction and the magnetic field $\boldsymbol{H}$ (in the Heaviside-Lorentz system of units). Furthermore we assume that the backround dielectric constant ϵ_r should not vary in time (only be spatially dependent) and of scalar nature. These assumptions lead to the following equations describing the coupled spatio-temporal dynamics of the three fields $\boldsymbol{E}$ (the electric field), $\boldsymbol{D}$ (the electric displacement field) and $\boldsymbol{H}$ (the magnetic field):

$$\nabla \times \boldsymbol{H}(\boldsymbol{r},t) = c^{-1}\,\frac{\partial\,\boldsymbol{D}(\boldsymbol{r},t)}{\partial t}, \qquad \nabla \times \boldsymbol{E}(\boldsymbol{r},t) = -c^{-1}\,\frac{\partial\,\boldsymbol{H}(\boldsymbol{r},t)}{\partial t} \tag{5.1}$$

$$\boldsymbol{D}(\boldsymbol{r},t) = \epsilon_\mathrm{r}(\boldsymbol{r})\,\boldsymbol{E}(\boldsymbol{r},t) + \boldsymbol{p}(\boldsymbol{r},t) \tag{5.2}$$

The polarisation density $\boldsymbol{p}$ is the link to the (spatio-temporal) material properties. The implementation of those will be discussed in the second part.

In 1966, Yee [5.2] presented a formulation for solving the Maxwell curl equations 5.1 in a discretised way. The algorithm named after him is highly efficient and still rather accurate. To translate the differentials in the Maxwell equations, Yee made use of a straightforward approach for the difference approximation of second order accuracy in δs, exemplified in 5.3. The differential at the position p is approximated by the difference quotient of the two neighbouring values at half-step distances

$$\left.\frac{\partial f(s)}{\partial s}\right|_{s=p} \rightarrow \lim_{\delta s \rightarrow 0} \frac{f(p+\delta s/2) - f(p-\delta s/2)}{\delta s}. \tag{5.3}$$

In these (from the point of view of the Maxwell equations "auxiliary") equations for the description of material properties, the use of an averaging rule is necessary, as a field value is not calculated for a certain time step. The following equation will be used in this case:

$$f(t) \rightarrow \lim_{\delta t \rightarrow 0} \frac{f(t+\delta t/2) + f(t-\delta t/2)}{2} \tag{5.4}$$

When carrying out the differencing it is essential to avoid as many averaging procedures as possible to achieve a high numerical stability.

The field values in the equations in discrete form will be labeled in a special way to make the appearance short and concise. Therefore we introduce a notation for field values F at certain positions in Cartesian space x, y, z and time t. The discrete field values should be pinned on an evenly spaced grid with a spatial stepping of δs and a temporal stepping of δt. Offsets can be changed as necessary.

$$F|^{m}_{i,j,k} := F(i\,\delta s, j\,\delta s, k\,\delta s, m\,\delta t) = F(x, y, z, t) \tag{5.5}$$

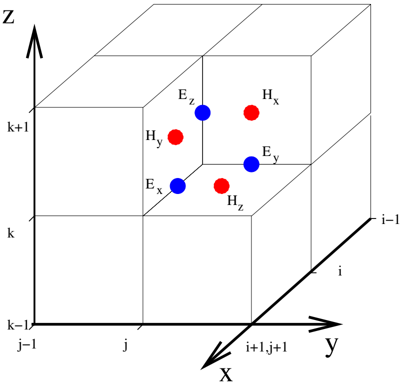

Fig. 5.1. The "Yee cube" showing the distribution of the field vector components in one grid cell at space point i, j, k. Shown are the Cartesian components of the electric (E) and the magnetic (H) fields.

```
void calcH () {
 for (int i = isc; i < iec; i++) {
  for (int j = jsc; j < jec; j++) {
   for (int k = ksc; k < kec; k++) {
    H_x(i,j,k) -= cdtds * ( E_z(i,j+1,k) - E_z(i,j,k) -
                            E_y(i,j,k+1) + E_y(i,j,k) );
    H_y(i,j,k) -= cdtds * ( E_x(i,j,k+1) - E_x(i,j,k) -
                            E_z(i+1,j,k) + E_z(i,j,k) );
    H_z(i,j,k) -= cdtds * ( E_y(i+1,j,k) - E_y(i,j,k) -
                            E_x(i,j+1,k) + E_x(i,j,k) );
   }
  }
 }
}
```

Fig. 5.2. Pseudo code realisation of the algorithm calculating the evolution of the magnetic field. The global constants `isc,` `jsc` and `ksc` define the lower bound of the core region of the simulation. `iec,` `jec` and `kec` define the upper bounds of the core region. The global constant `cdtds` is the factor $c \cdot \delta t / \delta s$. The global grid variables `H` and `E` represent the electric and magnetic fields.

The result of the translation to difference form of the Maxwell curl equations 5.1 is given in 5.6. For brevity, we only show the equation for the first Cartesian component x of the updating equation for the electric displacement field $\boldsymbol{D}$. The other five scalar equations that complete the curl equation set are of similar form and can be easily deduced.

$$D_x\Big|^{m+\frac{1}{2}}_{i+\frac{1}{2},j,k} = D_x\Big|^{m-\frac{1}{2}}_{i+\frac{1}{2},j,k} + \frac{c\,\delta t}{\delta s}\Bigg[\Big(H_z\Big|^{m}_{i+\frac{1}{2},j+\frac{1}{2},k} - H_z\Big|^{m}_{i+\frac{1}{2},j-\frac{1}{2},k}\Big) - \Big(H_y\Big|^{m}_{i+\frac{1}{2},j,k+\frac{1}{2}} - H_y\Big|^{m}_{i+\frac{1}{2},j,k-\frac{1}{2}}\Big)\Bigg] \tag{5.6}$$

Translating this into a pseudo programming language is straight forward. The algorithm is composed of two parts. One part is the calculation of the new electric displacement field (Fig. 5.3) and the other results in the new magnetic field (Fig. 5.2).

A very important aspect to consider in practice is the order of storage of the three dimensional arrays in memory. The innermost loop (k in the examples) should belong to the fastest index in the array. This means consecutive iterations for the index of this dimension should access neighbouring positions in memory. The cache architecture of the computer can then preload several array elements from the slower main memory needed in successive calculations all at once. The following iterations can then be executed with fast cache access.

An interesting detail of the Yee algorithm is the spatial distribution of the grid points as well as their temporal distribution. These spatial positions are

```
void calcD () {
 for (int i = isc; i < iec; i++) {
  for (int j = jsc; j < jec; j++) {
   for (int k = ksc; k < kec; k++) {
    D_x(i,j,k) += cdtds * ( H_z(i,j,k) - H_z(i,j-1,k) -
                            H_y(i,j,k) + H_y(i,j,k-1) );
    D_y(i,j,k) += cdtds * ( H_x(i,j,k) - H_x(i,j,k-1) -
                            H_z(i,j,k) + H_z(i-1,j,k) );
    D_z(i,j,k) += cdtds * ( H_y(i,j,k) - H_y(i-1,j,k) -
                            H_x(i,j,k) + H_x(i,j-1,k) );
   }
  }
 }
}
```

Fig. 5.3. Pseudo code realisation of the algorithm calculating the evolution of the electric displacement field. In addition to the global parameters introduced in calcH (Fig. 5.2), the global grid `D` represents the electric displacement field.

usually visualized on the so called Yee cube (Fig. 5.1), a three dimensional rectangular grid displaying the positions of the field values.

The electric displacement $\boldsymbol{D}$ and the magnetic induction $\boldsymbol{B}$ are at the positions of their appertaining fields $\boldsymbol{E}$ and $\boldsymbol{H}$, which are shown in the Yee cube. Similarly, the polarisation density $\boldsymbol{p}$ is situated at the position of the electric field and the electric displacement field.

The discretisation of the material equation 5.2, relating the electric field $\boldsymbol{E}$ to the electric displacement field $\boldsymbol{D}$ and the polarisation density $\boldsymbol{p}$ represents no further difficulty, as all field values are given at the same positions in space and time. A pseudo code implementation is shown in Fig. 5.4.

```
void calcE () {
 for (int i = isc; i < iec; i++) {
  for (int j = jsc; j < jec; j++) {
   for (int k = ksc; k < kec; k++) {
    E_x(i,j,k) = InvEps_x(i,j,k) * D_x(i,j,k);
    E_y(i,j,k) = InvEps_y(i,j,k) * D_y(i,j,k);
    E_z(i,j,k) = InvEps_z(i,j,k) * D_z(i,j,k);
   }
  }
 }
}
```

Fig. 5.4. Pseudo code realisation of the algorithm calculating the evolution of the electric field. The global grid `InvEps` represents the inverse of the ϵ_r material index. The different Cartesian indices `x`, `y` and `z` account for the spatial offset according to the Yee-cube.

We should point out that the use of three different grids for the inverse ϵ_{r} field is not mandatory. Only one grid is of real significance. Values of ϵ_{r} at the half-step points in space can be calculated by interpolation of neighbouring points as needed.

The Yee algorithm is highly efficient as only few and computationally fast operations (i.e. multiplications and sums) have to be processed. And it is still a rather accurate method to calculate the evolution of the electromagnetic fields in spite of using only approximations of second order accuracy in the differences. This fact can be attributed to the type of algorithm, called a half-time stepping or leap-frog type. This means that the algorithm leaps from the calculation of the new electric field, using the old magnetic field, to the calculation of the new magnetic field using the thus calculated magnetic field, and so on.

It can be shown that in d spatial dimensions the algorithm requires to satisfy the Courant condition

$$c \cdot \delta t \leq d^{-\frac{1}{2}} \cdot \delta s \tag{5.7}$$

in order to be stable. Another restriction has to be made for the spatial stepping δs. The wavelengths in the material with the highest diffraction index, which are to be investigated, should be represented by at least 12 grid points. This is a more strict application of the Nyquist criterion which has proven to be a good rule of thumb.

It should be mentioned here that there is a drawback of the method. Energy should be conserved by the basic Maxwell equations in free space. However, it turns out that the Yee algorithm is only energy conserving with respect to averaged values over longer times [5.5]. If strict energy conservation is required at all times higher orders of approximation for the differentials have been applied in simulations (see Taflove [5.6]).

5.3 Uniaxial Perfectly Matching Layers (UPML) Boundary Conditions

As the computational grid for the fields can not be infinite, they have to be terminated somewhere. The equations describing the termination are called boundary conditions. There are boundary conditions representing all kinds of real world systems. Metallic or closed boundary conditions are simple to implement, as the field value is just assumed to be vanishing at the position of the border. Electromagnetic waves are then totally reflected. A pseudo code implementation is given in Fig. 5.5. Periodic boundaries represent a certain kind of Bloch condition.

In our simulations we use open boundaries to model free space. Energy transmitted away from the object of interest by electromagnetic waves has to be lost. Moreover, there should be no feedback of energy from the borders

```
void calcPCW () {
 for (int k = 0; k < kmax; k++) {
  for (int i = 0; i < imax; i++) {
   E_z(i,0,k) = 0.;
   E_x(i,0,k) = 0.;
  }
  for (int j = 0; j < jmax; j++) {
   E_z(0,j,k) = 0.;
   E_y(0,j,k) = 0.;
  }
 }
 for (int j = 0; j < jmax; j++) {
  for (int i = 0; i < imax; i++) {
   E_y(i,j,0) = 0.;
   E_x(i,j,0) = 0.;
  }
 }
}
```

Fig. 5.5. Pseudo code realisation of the metallic boundary conditions. The tangential field values of the electric fields are set to 0. It is only necessary to do this on the lower bounds of the grid dimensions, as only these values are accessed. The global parameters `imax`, `jmax` and `kmax` are the upper bounds of the grid dimensions.

of the simulation region. It turned out that the so called Uniaxial Perfectly Matching Layers (U-PML) boundary condition is best suited for us.

The basic idea behind PML boundaries is to set up a region of conducting material which absorbs electromagnetic waves without reflection. As this region with the special material properties has to be terminated on the edge of

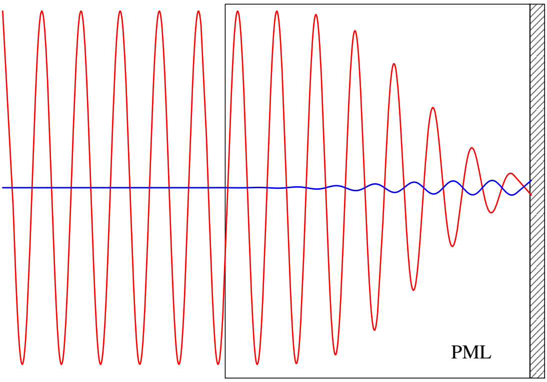

Fig. 5.6. A wave coming from the left enters the PML region and is dampened. It is reflected on the right by a perfectly conducting wall and passes the PML region again being still further absorbed.

the computational cube it is terminated with a totally reflecting boundary. The workings of such an enclosing PM layer is shown in Fig. 5.6. A wave coming from the left enters the PML. On the right side, the wave is totally reflected and crosses the PML again being further reduced in magnitude.

To describe such a behaviour in terms of the Maxwell equations in frequency space, the dielectric constant and the permeability have to be tensorial quantities. It turns out that both can be separated into a scalar and a tensorial part, with the tensorial part $\boldsymbol{s}$ being the same for both.

$$\begin{aligned} \nabla \times \boldsymbol{H} &= -\,\imath\omega\,\epsilon_{\mathrm{r}}\boldsymbol{s}\cdot\boldsymbol{E} \\ \nabla \times \boldsymbol{E} &= \quad \imath\omega\,\mu_{\mathrm{r}}\boldsymbol{s}\cdot\boldsymbol{H} \end{aligned} \tag{5.8}$$

The ansatz requiring a tensor $\boldsymbol{s}$ that absorbs an incoming wave without reflecting it leads to 5.9.

$$\boldsymbol{s} = \begin{bmatrix} \frac{s_y s_z}{s_x} & & 0 \\ & \frac{s_x s_z}{s_y} & \\ 0 & & \frac{s_x s_y}{s_z} \end{bmatrix} \qquad , s_i = \kappa_i - \frac{\sigma_i}{\imath\omega} \tag{5.9}$$

The parameters s_i — with i being one of x, y or z — can be separated into a real (κ_i) and an imaginary part (σ_i/ω). The real part degrades evanescent waves. The imaginary part absorbs energy.

The conversion of the differential equation 5.8 from frequency space to time-domain requires the introduction of two new fields $\boldsymbol{D}$ and $\boldsymbol{B}$ as shown in 5.10 to avoid the calculation of a convolution integral.

$$\boldsymbol{D} = \epsilon_{\mathrm{r}} \begin{bmatrix} \frac{s_z}{s_x} & & 0 \\ & \frac{s_x}{s_y} & \\ 0 & & \frac{s_y}{s_z} \end{bmatrix} \cdot \boldsymbol{E}; \qquad \boldsymbol{B} = \mu_{\mathrm{r}} \begin{bmatrix} \frac{s_z}{s_x} & & 0 \\ & \frac{s_x}{s_y} & \\ 0 & & \frac{s_y}{s_z} \end{bmatrix} \cdot \boldsymbol{H} \tag{5.10}$$

With this substitution, it is possible to separate the real and imaginary parts occurring on the right side of 5.8. The transformation to time-domain is then simply the substitution of $-\imath\omega$ by the time derivative.

$$\begin{aligned} \nabla \times \boldsymbol{H} &= \begin{bmatrix} \kappa_y & & 0 \\ & \kappa_z & \\ 0 & & \kappa_x \end{bmatrix} \cdot \frac{\partial \boldsymbol{D}}{\partial t} + \begin{bmatrix} \sigma_y & & 0 \\ & \sigma_z & \\ 0 & & \sigma_x \end{bmatrix} \cdot \boldsymbol{D} \\ \nabla \times \boldsymbol{E} &= - \begin{bmatrix} \kappa_y & & 0 \\ & \kappa_z & \\ 0 & & \kappa_x \end{bmatrix} \cdot \frac{\partial \boldsymbol{B}}{\partial t} - \begin{bmatrix} \sigma_y & & 0 \\ & \sigma_z & \\ 0 & & \sigma_x \end{bmatrix} \cdot \boldsymbol{B} \end{aligned} \tag{5.11}$$

$$\begin{aligned}
&\begin{bmatrix}\kappa_x & & 0\\ & \kappa_y & \\ 0 & & \kappa_z\end{bmatrix}\cdot\frac{\partial\boldsymbol{D}}{\partial t}+\begin{bmatrix}\sigma_x & & 0\\ & \sigma_y & \\ 0 & & \sigma_z\end{bmatrix}\cdot\boldsymbol{D}=\\
&\qquad\epsilon_{\mathrm{r}}\left\{\begin{bmatrix}\kappa_z & & 0\\ & \kappa_x & \\ 0 & & \kappa_y\end{bmatrix}\cdot\frac{\partial\boldsymbol{E}}{\partial t}+\begin{bmatrix}\sigma_z & & 0\\ & \sigma_x & \\ 0 & & \sigma_y\end{bmatrix}\cdot\boldsymbol{E}\right\}\\
&\begin{bmatrix}\kappa_x & & 0\\ & \kappa_y & \\ 0 & & \kappa_z\end{bmatrix}\cdot\frac{\partial\boldsymbol{B}}{\partial t}+\begin{bmatrix}\sigma_x & & 0\\ & \sigma_y & \\ 0 & & \sigma_z\end{bmatrix}\cdot\boldsymbol{B}=\\
&\qquad\mu_{\mathrm{r}}\left\{\begin{bmatrix}\kappa_z & & 0\\ & \kappa_x & \\ 0 & & \kappa_y\end{bmatrix}\cdot\frac{\partial\boldsymbol{H}}{\partial t}+\begin{bmatrix}\sigma_z & & 0\\ & \sigma_x & \\ 0 & & \sigma_y\end{bmatrix}\cdot\boldsymbol{H}\right\}
\end{aligned}\tag{5.12}$$

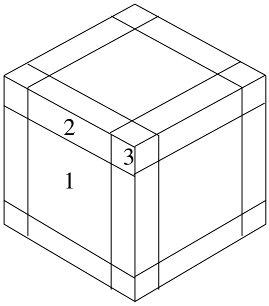

Fig. 5.7. The faces (1), edges (2) and corners (3) a PML has to be separated into.

An exemplary assembly of regions for the simulation is shown in Fig. 5.7. The inner core is surrounded by three types of PML layers which are finally terminated on the surface of the cube. As only that part of a wave travelling in the direction away from the center of the simulation should be absorbed, the fields components which are perpendicular to the faces of the cube should be effected. The PML has got a finite thickness, therefore edges and corners have to have more than one absorption coefficient to be present. On the faces of the cube, the waves should only be absorbed in the perpendicular direction, along the edges in both transverse directions. And in the corners the waves are to be absorbed in all directions. The conductivities and absorption coefficients σ_i and κ_i have to be set accordingly.

Discretisation of 5.11 and 5.12 is straightforward with respect to the discretisation rule (5.3). The results for the x component of the electric field and the displacement field update are shown in 5.13 and 5.14. Other components and field updates are of the same form and can easily be derived.

$$D_x\Big|_{i+\frac{1}{2},j,k}^{m+\frac{1}{2}} = \frac{\kappa_y - \frac{1}{2}\,\sigma_y\,\delta t}{\kappa_y + \frac{1}{2}\,\sigma_y\,\delta t}\, D_x\Big|_{i+\frac{1}{2},j,k}^{m-\frac{1}{2}} + \frac{\delta t}{\kappa_y + \frac{1}{2}\,\sigma_y\,\delta t} \cdot \left\{ \frac{H_z\big|_{i+\frac{1}{2},j+\frac{1}{2},k}^{m} - H_z\big|_{i+\frac{1}{2},j-\frac{1}{2},k}^{m}}{\delta s} - \frac{H_y\big|_{i+\frac{1}{2},j,k+\frac{1}{2}}^{m} - H_y\big|_{i+\frac{1}{2},j,k-\frac{1}{2}}^{m}}{\delta s} \right\} \tag{5.13}$$

$$E_x\Big|_{i+\frac{1}{2},j,k}^{m+\frac{1}{2}} = \frac{\kappa_z - \frac{1}{2}\,\sigma_z\,\delta t}{\kappa_z + \frac{1}{2}\,\sigma_z\,\delta t} E_x\Big|_{i+\frac{1}{2},j,k}^{m-\frac{1}{2}} + \frac{1}{\epsilon_{\mathrm{r}}} \left(\kappa_z + \frac{1}{2}\,\sigma_z\,\delta t\right)^{-1} \left\{ \left(\kappa_x + \frac{1}{2}\,\sigma_x\,\delta t\right) D_x\Big|_{i+\frac{1}{2},j,k}^{m+\frac{1}{2}} - \left(\kappa_x - \frac{1}{2}\,\sigma_x\,\delta t\right) D_x\Big|_{i+\frac{1}{2},j,k}^{m-\frac{1}{2}} \right\} \tag{5.14}$$

The pseudo code realisation of the above described and discretized algorithm is shown in Fig. 5.8. We restrict the presentation to the electric field part and leave the programming of the magnetic field calculation to the reader. What is missing in this code is the setup of the coefficient arrays ce_p (5.15 with $p \in \{x, y, z\}$) which is presented in Fig. 5.9. A similar setup has to be worked out for the magnetic field coefficient arrays.

$$\begin{aligned} ce_p(0,i) &= \kappa_p(i) + \frac{1}{2}\,\sigma_p(i)\,\delta t \\ ce_p(1,i) &= \left(\kappa_p(i) + \frac{1}{2}\,\sigma_p(i)\,\delta t\right)^{-1} \\ ce_p(2,i) &= \kappa_p(i) - \frac{1}{2}\,\sigma_p(i)\,\delta t \\ ce_p(3,i) &= \frac{\kappa_p(i) - \frac{1}{2}\,\sigma_p(i)\,\delta t}{\kappa_p(i) + \frac{1}{2}\,\sigma_p(i)\,\delta t} \end{aligned} \tag{5.15}$$

The implementation of just one highly absorbing sheath with a high absorption coefficient σ results in a large numerical error at the interface to the inner region. This error expresses itself in an artificial reflection. It turns out that the use of several layers with a smoothly increasing absorption coefficient resolves the problem. The same applies for the coefficient κ. A potential rising has proven to be a good approach and is shown in 5.16.

$$\sigma(x) = \sigma_{\max}\left(\frac{x}{d}\right)^p \qquad \kappa(x) = 1 + (\kappa_{\max} - 1)\left(\frac{x}{d}\right)^p \tag{5.16}$$

The parameter d is the thickness in layers of the boundary. The exponent p and the values for $\sigma_{\max}$ and $\kappa_{\max}$ can be freely chosen. Taflove shows in his excellent book on FDTD methods [5.6] that a choice for p between 3 and 4 gives reasonable results.

```
void calcPML_E () {
 calcPartPML_E(0, isc, 0, jmax, 0, kmax);
 calcPartPML_E(iec, imax, 0, jmax, 0, kmax);
 calcPartPML_E(isc, iec, 0, jsc, 0, kmax);
 calcPartPML_E(isc, iec, jec, jmax, 0, kmax);
 calcPartPML_E(isc, iec, jsc, jec, 0, ksc);
 calcPartPML_E(isc, iec, jsc, jec, kec, kmax);
}

void calcPartPML_E (int is, int ie,
                    int js, int je,
                    int ks, int ke) {
 float Dold_x, Dold_y, Dold_z;

 for (int i = is; i < ie; i++) {
  for (int j = js; j < je; j++) {
   for (int k = ks; k < ke; k++) {
    Dold_x = D_x(i,j,k);
    Dold_y = D_y(i,j,k);
    Dold_z = D_z(i,j,k);

    D_x(i,j,k) = ce_y(3,j) * Dold_x + dtds * ce_y(1,j) *
                 ( H_z(i,j,k) - H_z(i,j-1,k) -
                   H_y(i,j,k) + H_y(i,j,k-1) );
    D_y(i,j,k) = ce_z(3,k) * Dold_y + dtds * ce_z(1,k) *
                 ( H_x(i,j,k) - H_x(i,j,k-1) -
                   H_z(i,j,k) + H_z(i-1,j,k) );
    D_z(i,j,k) = ce_x(3,i) * Dold_z + dtds * ce_x(1,i) *
                 ( H_y(i,j,k) - H_y(i-1,j,k) -
                   H_x(i,j,k) + H_x(i,j-1,k) );

    E_x(i,j,k) = ce_z(3,k) * E_x(i,j,k) + ce_z(1,k)*InvEps_x(i,j,k) *
                 ( ce_x(0,i) * D_x(i,j,k) - ce_x(2,i) * Dold_x );
    E_y(i,j,k) = ce_x(3,i) * E_y(i,j,k) + ce_x(1,i)*InvEps_y(i,j,k) *
                 ( ce_y(0,j) * D_y(i,j,k) - ce_y(2,j) * Dold_y );
    E_z(i,j,k) = ce_y(3,j) * E_z(i,j,k) + ce_y(1,j)*InvEps_z(i,j,k) *
                 ( ce_z(0,k) * D_z(i,j,k) - ce_z(2,k) * Dold_z );
   }
  }
 }
}
```

Fig. 5.8. One part of a pseudo code realisation of the U-PML boundary condition. The global parameter `dtds` is $\delta t/\delta s$. The global parameter arrays `ce_x`, `ce_y` and `ce_z` have to be set up once initially.

He also shows that the reflection coefficient R (which is dependent on the angle φ of the incoming wave) can be approximated by 5.17.

$$R(\varphi) = \exp\left[-2\eta_{\mathrm{fs}}\,\epsilon_{\mathrm{r}}\,\cos\varphi\int_0^d \sigma(x)dx\right] \tag{5.17}$$

```
void setupPMLcoeff_E (vector ce, vector cm,
                      int ls, int le, int lmax) {
 vector val1(-1, PMLMAX-1, 1.);
 vector val2(-1, PMLMAX-1, 1.);
 vector val1p(-1, PMLMAX-1, 1.);
 vector val2p(-1, PMLMAX-1, 1.);

 for (int l = 0; l < pmlmax; l++) {
  x = float(l) / float(pmlmax);
  sigma = SigmaMax * pow(x,POTPML);
  kappa = 1. + (KappaMax - 1.) * pow(x,POTPML);
  val1(l) = kappa + 0.5 * sigma * dt;
  val2(l) = kappa - 0.5 * sigma * dt;

  x = (float(l) + 0.5) / float(PMLMAX-1)
  sigma = SigmaMax * pow(x, POTPML);
  kappa = 1. + (KappaMax - 1.) * pow(x,POTPML);
  val1p(l) = kappa + 0.5 * sigma * dt;
  val2p(l) = kappa - 0.5 * sigma * dt;
 }

 for (int l = 0; l < ls; l++) {
  ce(0,l) = val1p(ls - l - 2); ce(2,l) = val2p(ls - l - 2);
  ce(1,l) = 1. / val1(ls - l - 1);
  ce(3,l) = val2(ls - l - 1) / val1(ls - l - 1);

  cm(0,l) = val1(ls - l - 1); cm(2,l) = val2(ls - l - 1);
  cm(1,l) = 1. / val1p(ls - l - 2);
  cm(3,l) = val2p(ls - l - 2) / val1p(ls - l - 2);
 }

 for (int l = le; l < lmax; l++) {
  ce(0,l) = val1p(l - le); ce(2,l) = val2p(l - le);
  ce(1,l) = 1. / val1(l - le);
  ce(3,l) = val2(l - le) / val1(l - le);

  cm(0,l) = val1(l - le); cm(2,l) = val2(l - le);
  cm(1,l) = 1. / val1p(l - le);
  cm(3,l) = val2p(l - le) / val1p(l - le);
 }
}
```

Fig. 5.9. The setup routine of the ce_i and cm_i coefficient arrays. It has to be called for each dimension (x, y and z) with the matrices of coefficients. Both coefficient matrices ce and cm for each dimension have to have a range from 0 to 3 for the first index and the second index should be defined from 0 to the number of grid points in that dimension. The parameters `ls,` `le` and `lmax` are the starting, the end grid points of the core region, and the number of grid points respectively.

The impedance in free space is $\eta_{\mathrm{fs}} \approx 733\Omega$. This reflectivity has to be minimised leading to an optimal value for $\sigma_{\max}$. The aim is to adjust the parameters of the PMLs in such a way that the wave is damped as much as possible while keeping the numerical reflection error low.

5.4 Time-Domain Full Vectorial Maxwell-Bloch Equations

The coupling of material properties to the equations describing the behaviour of the electromagnetic fields in the framework discussed here is established by the functional dependence of the electric displacement D on the electric field E. Here we will restrict ourselves to a simple two level atomic system that is described by the dipolar interaction Hamiltonian with the electromagnetic field. The quantum mechanical behaviour of such an atomic system is described by complex pseudo-spin equations. Maxwell's (real valued) equations 5.1 have to be coupled to these. This was done in an approach first published by Ziolkowski *et al.* [5.3]. Here, we will present an alternative approach that follows the ideas that have been suggested by Nagra and York in 1998 [5.1]. As we will show in Appendix A, both models share the same functionality.

In the case of an atom with a dipolar interaction Hamiltonian, the functional dependence of $\boldsymbol{D}$ on $\boldsymbol{E}$ reads:

$$\boldsymbol{D}(\omega) = (1 + \boldsymbol{\chi}_{\mathrm{Lorentz}}(\omega))\ \epsilon_{\mathrm{r}}\ \boldsymbol{E}(\omega) \tag{5.18}$$

The factor $\chi_{\mathbf{Lorentz}}(\omega)$ represents the Lorentz line shape.

The susceptibility χ_{Lorentz} can be separated into two parts, being either entirely real χ' or imaginary χ''. They are given in5.19. Absorption is described by the imaginary part (as can be seen in Fig. 5.10); the associated phase shift specified by the real part of χ is shown in Fig. 5.12.

$$\begin{aligned} \chi'(\omega) &\sim \frac{\omega_0 - \omega}{\frac{1}{\omega}\left(\omega_0^2 - \omega^2\right)^2 + 4\omega\gamma^2} \\ \chi''(\omega) &\sim \frac{2\gamma}{\left(\frac{\omega_0^2}{\omega} - \omega\right)^2 + 4\gamma^2} \end{aligned} \tag{5.19}$$

The differential equation that describes this functional dependence is of the form of a damped harmonic oscillator equation (5.20).

$$\ddot{\boldsymbol{p}} + 2\gamma\,\dot{\boldsymbol{p}} + \omega_0^2\,\boldsymbol{p} = \underbrace{2\frac{\omega_0^2}{\mathit{\Omega}}\frac{1}{\hbar}\cdot|\boldsymbol{d}_{\mathbf{cv}}|^{\mathbf{2}}}_{\boldsymbol{\alpha}}\cdot\boldsymbol{E}\cdot(n + n_{\mathrm{a}}N_0) \tag{5.20}$$

It is enhanced by a highly nonlinear coupling to the inversion density n. n_{a} is the density of atoms in the material. They are characterised by the damping factor γ which is related to the line width and the resonance frequency $\mathit{\Omega}$. Both are related to the frequency ω_0 by

$$\mathit{\Omega}^2 = \omega_0^2 - \gamma^2. \tag{5.21}$$

The driving term on the right hand side of 5.20 that also characterises the atomic light field interaction, contains a coupling constant $\boldsymbol{\alpha}$, the electric

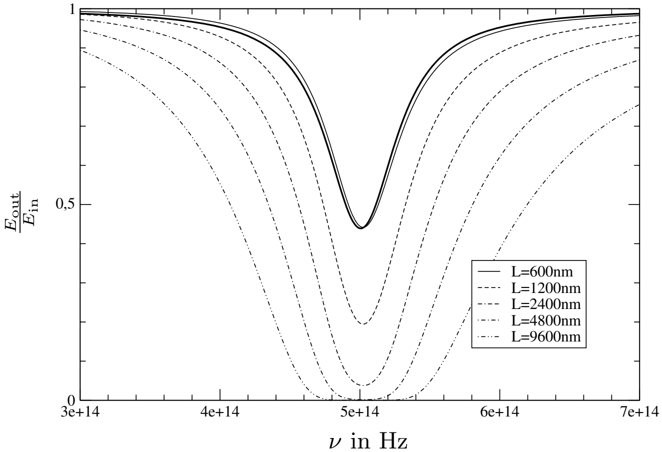

Fig. 5.10. The absorption spectra of a pulse travelling different distances in an initially absorbing active Lorentzian medium. See text.

field strength E at the position of the atom and the atomic inversion density n. The coupling constant $\boldsymbol{\alpha}$ includes the dipole matrix element $|\boldsymbol{d}_{\text{cv}}|^2$ that determines the strength and spatial orientation of the polarisation to the light-field coupling. The atomic inversion density n

$$n = n_{\text{a}} \left(\rho_{\text{aa}} - \rho_{\text{bb}}\right) \tag{5.22}$$

is related to the diagonal density matrix elements ρ_{aa} and ρ_{bb} of the quantum mechanical system with a lower level a and an upper level b. It represents the occupation of these.
N_0 is related to the equilibrium occupation ρ_0 of the upper, more energetic level, in the following way:

$$N_0 = 1 - 2\rho_0 \tag{5.23}$$

An equation of a form similar to the Einstein rate equations can be rigidly obtained from quantum mechanically derived optical Bloch equations for a two level system. Equation 5.24 describes the temporal evolution of the damped inversion density for a pumped two level system interacting with the electric field.

$$\dot{n} = -2n_{\text{a}}\Lambda - \gamma_{\text{nr}}n - 2\frac{\Omega}{\hbar\omega_0^2}\,\dot{\boldsymbol{p}} \cdot \boldsymbol{E} \tag{5.24}$$

A pumping term with pump strength Λ is included in the rate equation for the inversion density n. The term with the relaxation constant γ_{nr} represents a non-radiative relaxation of excited systems.
The term proportional to $\dot{\boldsymbol{p}} \cdot \boldsymbol{E}$ stands for the work of the electromagnetic field done on the active material in quanta of approximately $\hbar\omega_0$.

Equations 5.20 and 5.24 together with 5.1 and 5.2 form the already mentioned "auxiliary differential equation" (ADE) FDTD algorithm to simulate active material interacting with the electromagnetic field. The difference form of the material equations are given in 5.25 and 5.26.
As a full tensorial expression for $\boldsymbol{\alpha}$ would make the presentation very long and nontransparent we will assume in the following a diagonal form of $\boldsymbol{\alpha}$. Note that the spatial centering of the grids given in the equation below for the inversion density is not fully correct. In principle, the field values for $\boldsymbol{p}$ and $\boldsymbol{E}$ would have to be averaged on a central point in space. And this value should then be averaged back to the space point that is required in the polarisation equation. As the error due to this incorrect centering is of minor importance in most simulations, we simplify the given equations.

$$\begin{aligned} p_x\big|^{m+\frac{1}{2}} = \;& \frac{2-\omega^2\,\delta t^2}{1+\gamma\,\delta t}\cdot p_x\big|^{m-\frac{1}{2}} \\ & -\frac{1-\gamma\,\delta t}{1+\gamma\,\delta t}\cdot p_x\big|^{m-\frac{3}{2}} \\ & +\alpha_x\frac{\delta t^2}{1+\gamma\,\delta t}\cdot E_x\big|^{m-\frac{1}{2}}\cdot\left(n\big|^{m-\frac{1}{2}}+n_{\mathrm{a}}N_0\right) \end{aligned} \tag{5.25}$$

$$\begin{aligned} n\big|^{m+\frac{1}{2}} = \;& \frac{2-\gamma_{\mathrm{nr}}\delta t}{2+\gamma_{\mathrm{nr}}\delta t}\cdot n\big|^{m-\frac{1}{2}} \\ & -4\frac{\delta t}{2+\gamma_{\mathrm{nr}}\delta t}\cdot n_{\mathrm{a}}\Lambda \\ & -2\frac{\Omega}{(2+\gamma_{\mathrm{nr}}\delta t)\,\hbar\omega^2}\left\{\left(p_x\big|^{m+\frac{1}{2}}-p_x\big|^{m-\frac{1}{2}}\right)\cdot\right. \\ & \left(E_x\big|^{m+\frac{1}{2}}+E_x\big|^{m-\frac{1}{2}}\right)+ \\ & \left(p_y\big|^{m+\frac{1}{2}}-p_y\big|^{m-\frac{1}{2}}\right)\cdot \\ & \left(E_y\big|^{m+\frac{1}{2}}+E_y\big|^{m-\frac{1}{2}}\right)+ \\ & \left(p_z\big|^{m+\frac{1}{2}}-p_z\big|^{m-\frac{1}{2}}\right)\cdot \\ & \left.\left(E_z\big|^{m+\frac{1}{2}}+E_z\big|^{m-\frac{1}{2}}\right)\right\} \end{aligned} \tag{5.26}$$

To complete the model the electric field values E from the Maxwell equations in Heaviside-Lorentz units have to be divided by ϵ_0 to link them with the above equations for the material system in the MKSA unit system.

In the pseudo code implementation shown in Fig. 5.11 the constant values `PFA, PFB, PFC, NFA, NFB` and `NFC` represent the values given in 5.27.

$$
\begin{aligned}
PFA =& \frac{2-\omega^2\,\delta t^2}{1+\gamma\,\delta t} \\
PFB =& \frac{1-\gamma\,\delta t}{1+\gamma\,\delta t} \\
PFC_i =& \alpha_i \frac{\delta t^2}{1+\gamma\,\delta t}\frac{1}{\epsilon_0} \\
NFA =& \frac{2-\gamma_{\mathrm{n}r}\delta t}{2+\gamma_{\mathrm{n}r}\delta t} \\
NFB =& -4\frac{\delta t}{2+\gamma_{\mathrm{n}r}\delta t}\cdot n_{\mathrm{a}}\Lambda \\
NFC =& -2\frac{\Omega}{(2+\gamma_{\mathrm{n}r}\delta t)\,\epsilon_0\hbar\omega^2}
\end{aligned}
\tag{5.27}
$$

The auxiliary equations do not impose any further restrictions on the stability rules for the simulation.

5.5 Computational Costs

The computing resources that one can use for the simulation of physical systems place a few restrictions on the system geometries and time scales to be investigated. Memory (especially the fast memory) is only available in restricted quantities. And processors always seem to be too slow to satisfy the demands of huge grid sizes.

To calculate a rough estimate of the amount of memory that is required for a simulation run we may resort to the following equation that gives an estimate of the required space S in bytes.

$$
S \approx w \cdot \left[\underbrace{N^3 \cdot f_{\mathrm{c}}}_{\text{core}} + \underbrace{12 \cdot p \cdot N^2}_{\text{PML}}\right] \tag{5.28}
$$

The parameter w should be the number of bytes for one word, meaning the size of a floating point number. N stands for the number of grid points of one side of the simulation cube, with f_{c} required values per grid point in the core region. The perfectly matching boundary should be made of p layers with f_{p} values per grid point.

In the boundary region there have to be 12 arrays for the 4 physical quantities and their 3 Cartesian components. In the core region, the 6 components of the electric and magnetic fields come along with 3 components for the electric displacement field. If active material is present, 1 value per grid point for the inversion density and 6 values for the present and former polarisation components (as it is a differential equation of second order) have to be stored. In the pseudo code implementation 3 additional values for the old electric field components have to be stored. If the background dielectric

```
void calcPN () {
 float Ps_x, Ps_y, Ps_z;
 for (int i = isa; i < iea; i++) {
  for (int j = jsa; j < jea; j++) {
   for (int k = ksa; k < kea; k++) {
    Ps_x = P_x(i,j,k); Ps_y = P_y(i,j,k); Ps_z = P_z(i,j,k);

    P_x(i,j,k) = PFA * P_x(i,j,k) -
                 PFB * Po_x(i,j,k) +
                 PFC_x * Eo_x(i,j,k) * ( N(i,j,k) - N_0 );
    P_y(i,j,k) = PFA * P_y(i,j,k) -
                 PFB * Po_y(i,j,k) +
                 PFC_y * Eo_y(i,j,k) * ( N(i,j,k) - N_0 );
    P_z(i,j,k) = PFA * P_z(i,j,k) -
                 PFB * Po_z(i,j,k) +
                 PFC_z * Eo_z(i,j,k) * ( N(i,j,k) - N_0 );

    Po_x(i,j,k) = Ps_x; Po_y(i,j,k) = Ps_y; Po_z(i,j,k) = Ps_z;

    E_x(i,j,k) -= InvEps_x(i,j,k) * P_x(i,j,k);
    E_y(i,j,k) -= InvEps_y(i,j,k) * P_y(i,j,k);
    E_z(i,j,k) -= InvEps_z(i,j,k) * P_z(i,j,k);

    N(i,j,k) = NFA * N(i,j,k) +
               NFB +
               NFC * ( ( P_x(i,j,k) - Po_x(i,j,k) ) *
                       ( E_x(i,j,k) + Eo_x(i,j,k) ) +
                       ( P_y(i,j,k) - Po_y(i,j,k) ) *
                       ( E_y(i,j,k) + Eo_y(i,j,k) ) +
                       ( P_z(i,j,k) - Po_z(i,j,k) ) *
                       ( E_z(i,j,k) + Eo_z(i,j,k) ) );
   }
  }
 }
}
```

Fig. 5.11. The routine calculating the material behaviour. The active region is bounded by `isa` to `iea-1`, `jsa` to `jea-1` and `ksa` to `kea-1`. The global grids `P` and `Po` are the current and former time step field representations for the polarisation density. `Eo` is the old electric field that is defined globally. `N` represents the inversion density. The other values are also globally defined constant parameters defined in the text.

constant ϵ varies in space then either 1 or 3 values per grid point — depending on the accuracy needed — have to be added. In total, f_c will thus range from 6 to 22 values per spatial grid point. Consequently, the amount of memory needed for such a simulation is enormous. The computer has to access each value every time step at least once. Unfortunately, modern computers have the problem that it is much more time consuming to access main memory than it takes to perform an operation. Therefore it is obvious that a computer with fast memory access is much more important than the time it takes to perform a multiplication or addition.

5.6 Test Runs

Various test runs were performed using on a one dimensional system with 3000 spatial grid points and a spatial cell length of $\delta s = 6\text{nm}$. The time stepping δt was chosen to obey equation 5.7.

In our computer simulations, the active medium has a resonance frequency of $\Omega = 5 \times 10^{14}\text{Hz}$ and a line width of $\Gamma = 2\gamma = \pi \times 10^{14}\text{s}^{-1}$.
The dipole matrix element in this cases is $|d_{\text{cv}}|^2 \approx 3.83 \times 10^{-58}\text{A s m}$ and the density of the atoms $n_{\text{a}} = 1 \times 10^{26}\text{m}^{-3}$. There is no pumping ($\Lambda = 0$) and the non-radiative recombination rate is set to $\gamma_{\text{nr}} = 5 \times 10^{7}\text{s}^{-1}$. Temporally narrow pulses are travelling through an active medium layer of different thicknesses L.

Initially, at $t = 0$, the medium is in its ground state ($n = n_{\text{a}}$) with the thermal equilibrium occupation of the upper state ρ_0 being 0. A pulse with an amplitude of $2.5 \times 10^{8}\text{V/m}$ small enough that the population of the atomic states is not noticeably changed is sent through an absorbing medium of different lengths. The system then responds in a linear way. The center frequency of the pulse with a Gaussian envelope was exactly the resonance frequency of the Lorentzian medium. The distance the pulses had to travel through the Lorentzian medium were $L \in \{600, 1200, 2400, 4800, 9600\text{nm}\}$ respectively.

The absorption spectra of the pulse for the 5 different path lengths are shown in Fig. 5.10. The theoretical absorption coefficient is given by:

$$\frac{E_{\text{out}}}{E_{\text{in}}} = \mathrm{e}^{-\frac{1}{2}\,\frac{\omega}{c}\chi''(\omega)L} \tag{5.29}$$

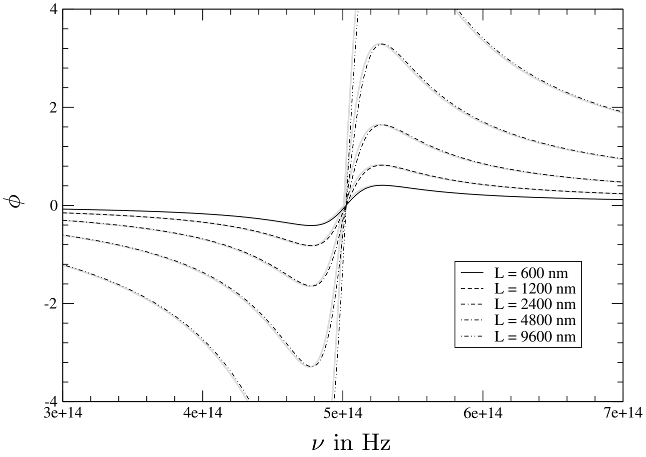

Fig. 5.12. The phase shift spectra of a pulse travelling different distances in an initially unexcited active Lorentzian medium.

The spectrum of the smallest absorption, belonging to the 600 nm path length is compared to the theoretical prediction of the absorption behaviour. A slight shift to higher frequencies of about 3 parts in a thousand occurs in the case of the numerically calculated result. The phase shift $\phi(\omega)$ of the pulse is shown in 5.12 for the same set of lengths L. The theoretical prediction to which it is compared reads:

$$\phi = -\frac{1}{2}\frac{\omega}{c}\chi'(\omega)L \tag{5.30}$$

With the length of the absorbing medium increasing, the dip of the absorption curve gets deeper and the phase shift larger. Eventually the dip reaches 0, which means total absorption. The phase shift spectra are compared to the theoretical prediction of the absorption behaviour. As Fig. 5.12 shows, the analytic expression corresponds very well with our numerical results.

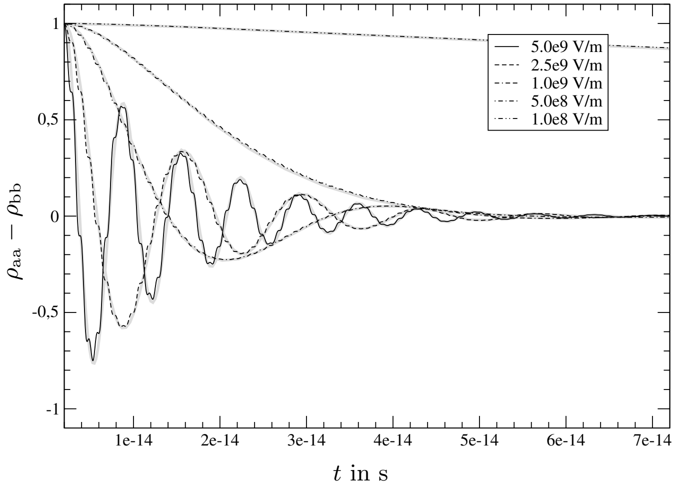

Fig. 5.13. Electromagnetic waves of different amplitudes drive a decaying Rabi oscillation to a steady state where neither light is emitted nor absorbed by the medium.

To further test the auxiliary difference equations we analyze Rabi oscillations on the basis of the rate equation 5.24 describing the atomic inversion density. Rabi oscillations (see for example R. Loudon, "The quantum theory of Light" [5.4]) refer to an oscillating behaviour of the occupation probability of the atomic states interacting with coherent EM waves of one single frequency (Fig. 5.13). In our test-setup of an atomic system we assume that initially the atoms were unperturbed and entirely in their lower states. A wave of a certain amplitude $\hat{E}$, but with the resonance frequency Ω of the quantum mechanical two-level system, is then switched on. This simulation is repeated for 5 different amplitudes of the probing wave. The result is presented in Fig. 5.13.

A theoretical investigation of the occupation probability results in the prediction of the frequency and the decay rate for the Rabi oscillation given in 5.31.

$$\begin{aligned}
N(t) =&\rho_{\mathrm{aa}}(t) - \rho_{\mathrm{bb}}(t)\\
=&\begin{cases} e^{-\mathit{\Gamma}_{\mathrm{R}}t} \cdot \left[\cos \mathit{\Omega}_{\mathrm{R}}t \;\; + \frac{\mathit{\Gamma}_{\mathrm{R}}}{\mathit{\Omega}_{\mathrm{R}}} \sin \mathit{\Omega}_{\mathrm{R}}t\right] & \forall\, 4\omega_{\mathrm{R}}^2 > (\gamma - \gamma_{\mathrm{nr}})^2 \\ e^{-\mathit{\Gamma}_{\mathrm{R}}t} \cdot \left[\cosh \mathit{\Omega}_{\mathrm{R}}t + \frac{\mathit{\Gamma}_{\mathrm{R}}}{\mathit{\Omega}_{\mathrm{R}}} \sinh \mathit{\Omega}_{\mathrm{R}}t\right] & \forall\, 4\omega_{\mathrm{R}}^2 \le (\gamma - \gamma_{\mathrm{nr}})^2 \end{cases}\\
\mathit{\Omega}_{\mathrm{R}}^2 =&\frac{1}{4}\,(\gamma - \gamma_{\mathrm{nr}})^2 - \omega_{\mathrm{R}}^2 \\
\mathit{\Gamma}_{\mathrm{R}} =&\frac{1}{2}\,(\gamma + \gamma_{\mathrm{nr}})\\
\omega_{\mathrm{R}} =&\frac{\alpha \mathit{\Omega}}{2\hbar\omega_0^2}\hat{E}
\end{aligned} \tag{5.31}$$

So there are two cases. An oscillating one that is dampened and an over damped one that is not oscillating, but slowly relaxing to the steady state. In Fig. 5.13 this case is presented by the 1×10^8V/m and the 5×10^8V/m amplitudes, as opposed to the other 3 amplitudes.

A comparison of this theory with the numerical results shows good agreement. The fast periodic oscillations we obtain can be attributed to the simulation of the full dynamics in the algorithm versus the slowly varying amplitude approximation on which the analytic derivation is based.

As a further test we check the behaviour of a detuning in the frequency of the probing wave. In the simulations, we artificially reduce the line width

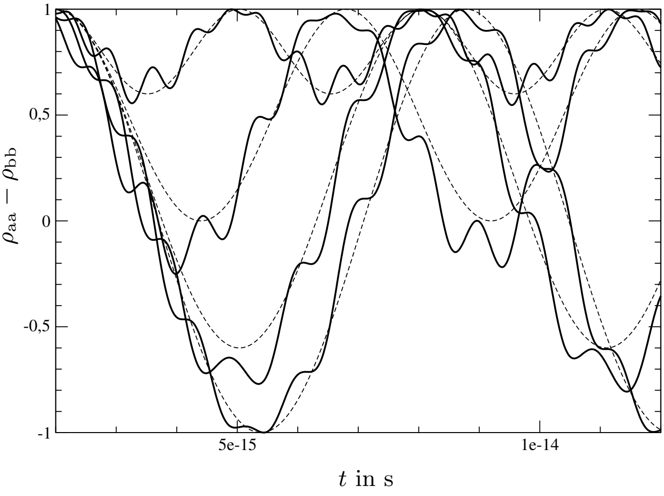

Fig. 5.14. Rabi flopping behaviour with 5 levels of frequency detuning.

of the dipole transition and the non radiative recombination rate γ_{nr} to zero. Thus the decay rate of the Rabi oscillation $\mathit{\Gamma}_{\mathrm{R}}$ vanishes. The amplitude of the probing wave is set to $\hat{E} = 5 \times 10^9 \mathrm{V/m}$. In the computer simulations, five different ratios of detuning from the resonance frequency $|\mathit{\Omega} - \omega|/\omega_{\mathrm{R}}$, (0, 0.5, 1, 2) were compared with the theoretical/analytical prediction. The simulation results (dashed) are shown in Fig. 5.14. Similar to the previous example, the results match very well the analytically predicted behaviour.

Figure 5.15 shows as a nice result of all of the above that the application of pulses with the length of half the period of a Rabi oscillation (a π pulse) inverts the occupation. Likewise, in the case of applying a pulse of the length of an entire Rabi oscillation period (2π pulse) the population of the lower level goes through a cycle of depopulation an repopulation.

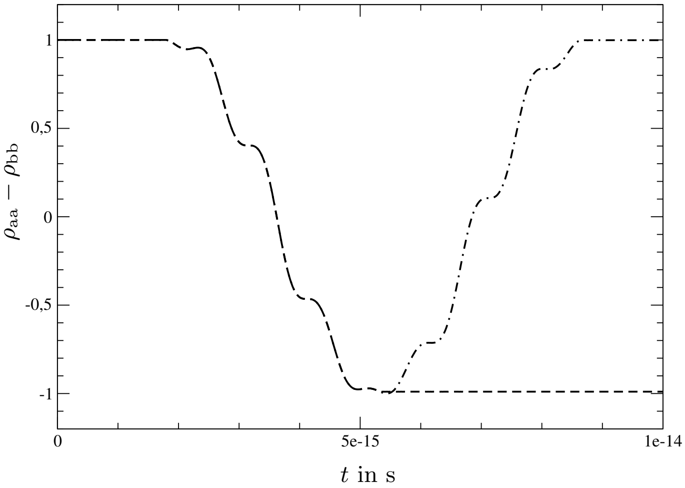

Fig. 5.15. Demonstration of the effect of so called π and 2π pulses (pulses of certain lengths) on the inversion density of the material system.

5.7 Microdisk Laser Dynamics

In contrast to the examples that we have considered so far (all of the above results were achieved using a one-dimensional code as presented by Nagra and York [5.1]) the microdisk resonator/laser (Fig. 5.16) that we will discuss in the following is (with respect to the computer simulation) a truly three-dimensional system. Figure 5.16 shows the essential features of a whispering gallery mode excited in a microdisk. These modes are the most intriguing attribute of electromagnetic fields in these cylindrical structures. They have their maximum field values on the circumference of the disk and can be

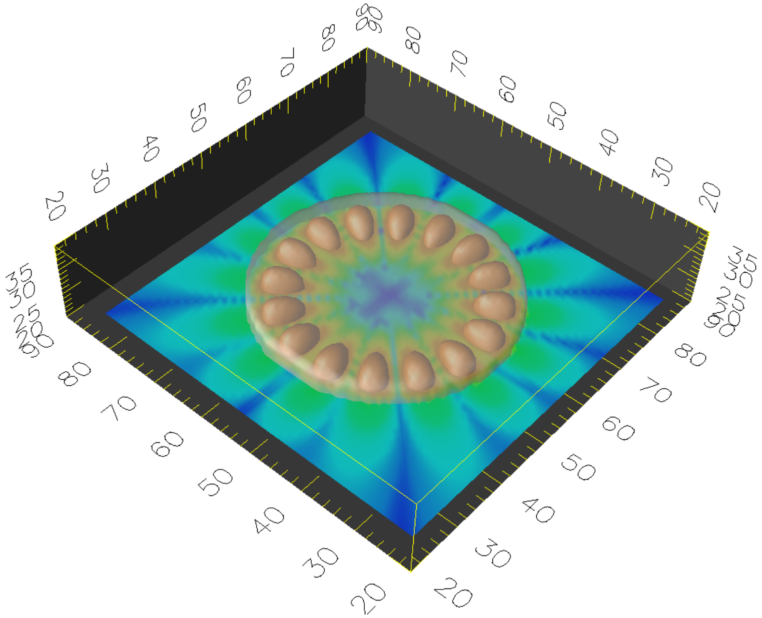

Fig. 5.16. A microdisk (hollow cylinder) showing the essential features of a $HEM_{8,1,0}$ whispering gallery mode. The features represent the isosurface of the z component of the magnetic field. The color plot shows component on a plane intersecting the disk in the middle.

characterised by the number of nodes in the azimuthal, the radial and the axial dimension. The mode shown in Fig. 5.16 is therefore a $HEM_{8,1,0}$ mode having 8 nodes around the disk, 1 node in the middle and 0 nodes in the axial direction.

Associated with every one of these modes in the disk is an eigen-frequency. If an active material inside the disk will support this frequency, strong emission of light could be achieved when pumping the respective quantum mechanical transition involved. The fact that these modes have high quality factors implies that they emit radiation very slowly. This makes them highly interesting for low threshold lasing devices.

Such a lasing device was simulated using the described ADE-FDTD algorithm in 3 spatial dimensions. The resonance frequency of the active Lorentzian medium was chosen to match the eigen-frequency of the $HEM_{4,1,0}$ mode of a microdisk with a radius of 105nm and a height of 30nm. The background material was chosen to have an ϵ_{r} of 11.1556. Pumping was homogeneous over the whole disk.

The result for the inversion density over time is plotted in Fig. 5.17. The upper curve gives the spatially averaged inversion density and the lower curve the inversion density at one point in the disk. The averaged inversion is higher than the inversion at the position of the whispering gallery mode as inversion is accumulating in the center due to the lack of a lasing center mode. After a few short relaxation oscillations, lasing sets in and the calculation reveals a rotation of the mode around the center of the disk.

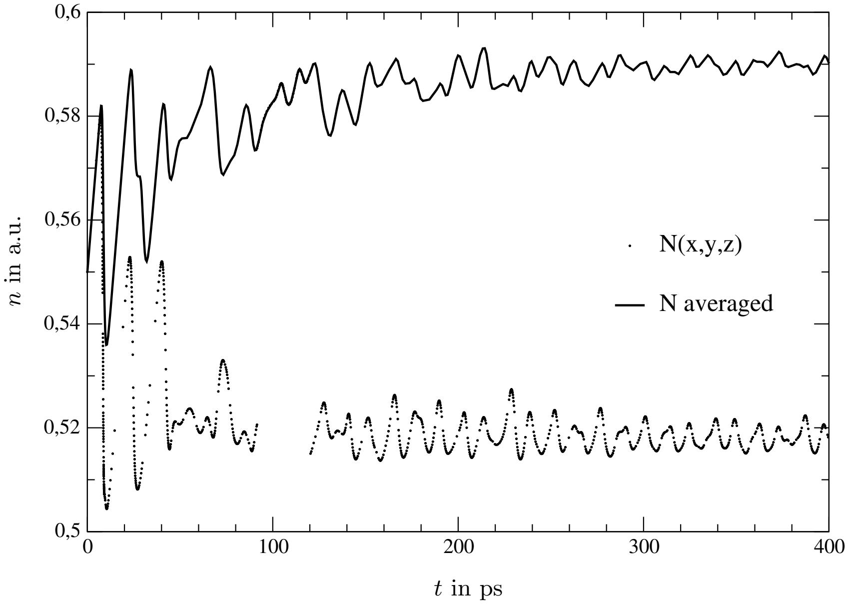

Fig. 5.17. Temporal inversion density plot from the simulation of lasing behaviour in a microdisk resonator filled with an excited two level atomic system active material. The inversion density is given in artificial units.

Figure 5.18 shows the inversion density n at an arbitrary time step in the simulation. Lasing at the eigen-frequency takes place and the associated $\mathrm{HEM}_{4,1,0}$ whispering gallery mode spatially consumes the inversion density at the rim of the disk. It is thus embossing the mode structure into the density profile. In the middle, the pumping piled up an inversion hill which is not touched by the whispering gallery modes. Occasionally, the inversion density in the middle is high enough to support a highly lossy $\mathrm{HEM}_{0,0,0}$ mode which then occurs for a very short period in time until the inversion density is again reduced below threshold.

As the "modes" in a nonlinear system are not fixed in space they can change their shape and position. With the inversion being, due to spatial hole burning, higher at the nodes of the modes the $\mathrm{HEM}_{4,1,0}$ mode starts to rotate in order to maximize its depletion of the available inversion.

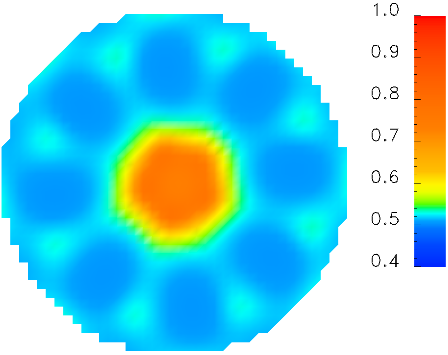

Fig. 5.18. Inversion density plot from a simulation of the lasing behaviour of a microdisk resonator filled with a pumped two level atomic system active material. The inversion density is given in artificial units.

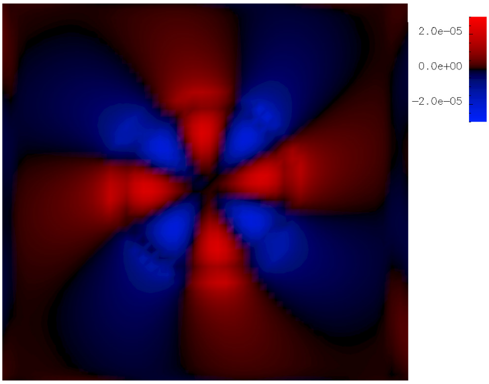

Fig. 5.19. Electric field color plot from a simulation of the lasing behaviour of a microdisk resonator filled with a pumped two level atomic system active material. The electric field strength is given in artificial units.

5.8 Conclusion

We have discussed a numerical method that unites finite-differnce time-domain (FDTD) computer simulations of active, nonlinear photonic nanomaterials with optical Bloch equations describing their microscopic spatio-temporal dynamics. Computationally simulated Rabi oscillations closely correspond to analytic results. Fully three-dimensional simulations reveal the nonlinear spatio-temporal dynamics of high-finesse whispering gallery modes in microdisk lasers. These are, in particular, dynamic, fan-like oscillation of the electromagnetic fields and inversion density of the WGM driven by spatial holeburning effects.

Appendix A: Relations

In this section, the relation between the Lorentz oscillator equation to the polarisation pseudo-spin equation of a electric dipole transitions will be shown. For simplicity we restrict the discussion to the scalar form of the equations, as the important aspects of the amplitude dynamics are not related to the vectorial character.
The harmonic oscillator differential equation is of second order with real values, whereas the pseudo-spin differential equations are of first order with complex values. Equation 5.32 is the optical Bloch equation (see for example in Loudon [5.4]) for the off-diagonal part of the density matrix ρ of a two level system, which is related to the polarisation. The upper level is labeled b, the lower one a.

$$\partial_t \rho_{\mathrm{ba}} = -\left(\gamma + \imath\,\Omega\right)\rho_{\mathrm{ba}} + \imath\frac{1}{\hbar} d \cdot E \cdot \left(\rho_{\mathrm{aa}} - \rho_{\mathrm{bb}}\right) \tag{5.32}$$

To demonstrate the relation of these two sets of equations, the Lorentz (or harmonic oscillator) 5.20 is first transfered into a system of differential equations of first order by introducing the new real quantity Q.

$$\begin{aligned} \partial_t P &= \qquad\qquad\quad Q \\ \partial_t Q &= -\,\omega_0^2 P - 2\gamma\, Q \quad + \alpha E N \end{aligned} \tag{5.33}$$

Subsequently, we then diagonalise this coupled system of first order differential equations with real variables P and Q and constants γ and ω_0. This leads to two uncoupled differential equations of first order with complex variables Π and Π^*, shown in 5.34. The two decoupled equations are complex conjugates of each other. We introduce a new frequency $\Omega = \sqrt{\omega_0^2 - \gamma^2}$ being a real quantity for $\omega_0 > \gamma$.

$$\begin{aligned} \partial_t \Pi \;\; &= -\left(\gamma + \imath\,\Omega\right)\Pi \;\; - \frac{\imath}{2\eta\Omega}\left(\gamma + \imath\,\Omega\right)\alpha E N \\ \partial_t \Pi^* &= -\left(\gamma - \imath\,\Omega\right)\Pi^* + \frac{\imath}{2\eta\Omega}\left(\gamma - \imath\,\Omega\right)\alpha E N \end{aligned} \tag{5.34}$$

The complex quantity Π is related to P and Q through the transformation matrix used in the diagonalisation. By normalising the eigen-vector of the equation system, an arbitrary constant η is introduced. To relate the value of Π to the polarisation P, η is chosen so that the real part of Π equals P and thus still represents the polarisation.

$$\Pi = -\frac{\imath\omega_0^2}{2\eta\Omega}\left(P + \frac{\gamma + \imath\,\Omega}{\omega_0^2} Q\right) \tag{5.35}$$

In the limit of $\gamma/\omega_0 \to 0$ and the particular choice of $\eta = -\imath\omega_0^2/\left(2\Omega\right)$, the diagonalised Lorentz differential system of 5.34 reduces to a form which closely matches the optical Bloch equation for the polarisation (5.32).

$$\partial_t \varPi = -\left(\gamma + \imath\, \varOmega\right) \varPi - \imath \frac{\varOmega}{\omega_0^2} \alpha E N \tag{5.36}$$

So the factor α is given by comparing the quantum mechanically derived equation to 5.36.

$$\alpha = \frac{\omega_0^2}{\hbar \varOmega} d \tag{5.37}$$

The second optical Bloch equation (5.38) describing the inversion $N := \rho_{\mathrm{aa}} - \rho_{\mathrm{bb}}$ of the two level system can then be directly translated to the real value space. Surely the system must be in any of the two levels, the sum of the probabilities of the system being in either one is normalised to $\mathrm{Tr}\left[\rho\right] = \rho_{\mathrm{aa}} + \rho_{\mathrm{bb}} := 1$.

$$\partial_t N = -\frac{4}{\hbar} d \cdot E \cdot \Im[\rho_{\mathrm{ba}}] \tag{5.38}$$

With the identification of $\varPi$ with ρ_{ba}, 5.35 and the norm $\eta = -\imath\omega_0^2 / \left(2\varOmega\right)$, the imaginary part of the off diagonal density matrix part is:

$$\Im[\rho_{\mathrm{ba}}] = \frac{\varOmega}{\omega_0^2} \partial_t P \tag{5.39}$$

So the temporal inversion evolution 5.38 transforms to the following form.

$$\partial_t N = -4 \frac{\varOmega}{\hbar \omega_0^2} d \cdot E \cdot \partial_t P \tag{5.40}$$

We will now finally introduce a few phenomenological terms. The inversion N should relaxate with a non radiative relaxation constant γ_{nr}, so that the steady state occupation probability ρ_0 of the upper level is reached. And there should be a possibility to non radiativly pump the upper level with a pumping rate $\varLambda$.

The non-radiative relaxation of the upper niveau for an unperturbed two-level system, with the relaxation rate γ_{nr} is given by the following rate equation.

$$\partial_t\, \rho_{\mathrm{bb}} \Big|_{\mathrm{nr}} = -\gamma_{\mathrm{nr}} \cdot \left(\rho_{\mathrm{bb}} - \rho_0\right) \tag{5.41}$$

It can easily be deduced, that the evolution of the inversion N for this relaxation behaviour is as follows:

$$\partial_t\, N \Big|_{\mathrm{nr}} = -\gamma_{\mathrm{nr}} \cdot \left(N - \left(1 - 2\rho_0\right)\right) = -\gamma_{\mathrm{nr}} \cdot \left(N - N_0\right) \tag{5.42}$$

The pumping of the upper niveau with a rate of $\varLambda$ can be expressed in the below equation for the inversion N:

$$\partial_t\, N \Big|_{\mathrm{pump}} = -2\varLambda \tag{5.43}$$

Combining those two additional terms and inserting them in 5.40 results in the following evolution equation for the inversion N.

$$\partial_t N = -4 \frac{\Omega}{\hbar\omega_0^2} d \cdot E \cdot \partial_t P - 2\Lambda - \gamma_{\mathrm{nr}} \cdot (N - N_0) \tag{5.44}$$

References

[5.1] Amit S. Nagra and Robert A. York. FDTD Analysis of Wave Propagation in Nonlinear Absorbing and Gain Media. *IEEE Transactions on Antennas and Propagation*, 46(3):334–340, March 1998. 1d adefdtd, 4 lvl atomic system, rate equations, pulse propagation.

[5.2] K. S. Yee. Numerical solution of initial boundary value problems involving Maxwell's equations in isotropic media. *IEEE Trans. Antennas Propag.*, 14:302–307, May 1966.

[5.3] Richard W. Ziolkowski, John M. Arnold, and Daniel M. Gogny. Ultrafast pulse interactions with two-level atoms. *Physical Review A*, 52(4):3082–3094, October 1995.

[5.4] Rodney Loudon. *The Quantum Theory of Light.* Oxford Science Publications, 1 edition, 1973.

[5.5] A. Taflove. *Computational Electrodynamics: The Finite-Difference Time-Domain Method.* Norwood, MA: Artech House, 1995.

[5.6] A. Taflove. *Advances in Computational Electrodynamics: The Finite-Difference Time-Domain Method.* Norwood, MA: Artech House, 1998.